Integrated TE and TM optical circulators on ultra-low-loss silicon nitride platform

Paolo Pintus,[1,*] Fabrizio Di Pasquale,[1] and John E. Bowers[2]

[1]*Scuola Superiore Sant'Anna, via Moruzzi 1, 56124 Pisa, Italy*
[2]*Department of Electrical and Computer Engineering, University of California, Santa Barbara, California 93106, USA*
[*]*paolo.pintus@sssup.it*

Abstract: In this paper, we present two four-port optical circulators for TE and TM modes, respectively. Exploiting the recent technological development concerning Ce:YIG pulse laser deposition on silicon nitride platform, we design two integrated circulators, which can be used to implement several functions in integrated optics, such as de-interleavers, input/output amplifier isolators and output laser isolators. The proposed devices combine the benefit of low loss silicon nitride waveguides with the non-reciprocal properties of magneto-optical materials. The ring cross-section has been optimized in order to maximize the non-reciprocal phase shift and finally the scattering coefficients have been computed using the transfer matrix method. The material stability and refractive index regularity of silicon nitride, the small micro-ring footprint, and the high wavelength selectivity make these devices particularly attractive.

OCIS codes: (230.3240) Isolators; (230.5750) Resonators; (230.3810) Magneto-optical devices.

References and links

1. T. R. Zaman, X. Guo, and R. J. Ram, "Semiconductor waveguide isolators," J. Lightwave Technol. **26**(2), 291–301 (2008).
2. N. Kono, K. Kakihara, K. Saitoh, and M. Koshiba, "Nonreciprocal microresonators for the miniaturization of optical waveguide isolators," Opt. Express **15**(12), 7737–7751 (2007).
3. Z. Wang and S. Fan, "Optical circulators in two-dimensional magneto-optical photonic crystals," Opt. Lett. **30**(15), 1989–1991 (2005).
4. W. Śmigaj, J. Romero-Vivas, B. Gralak, L. Magdenko, B. Dagens, and M. Vanwolleghem, "Magneto-optical circulator designed for operation in a uniform external magnetic field," Opt. Lett. **35**(4), 568–570 (2010).
5. R. Takei and T. Mizumoto, "Design and simulation of silicon waveguide optical circulator employing nonreciprocal phase shift," Jpn. J. Appl. Phys. **49**(5), 052203 (2010).
6. L. Bi, J. Hu, D.-H. Kim, G. F. Dionne, L. C. Kimerling, and C. A. Ross, "On-chip optical isolation in monolithically integrated non-reciprocal optical isolators," Nat. Photonics **5**(12), 758–762 (2011).
7. M. C. Onbasli, T. Goto, K. Taichi, H. Dong, L. Bi, and C. Ross, "Integration of magneto-optical cerium-doped YIG on silicon nitride films for nonreciprocal photonic devices," in *Frontiers in Optics*, OSA Technical Digest (online) (Optical Society of America, 2012), paper FTu1A.4.
8. D. D. John, M. J. R. Heck, J. F. Bauters, R. Moreira, J. S. Barton, J. E. Bowers, and D. J. Blumenthal, "Multilayer platform for ultra-low-loss waveguide applications," IEEE Photon. Technol. Lett. **24**(11), 876–878 (2012).
9. S.-Y. Sung, X. Qi, and B. J. Stadler, "Integrating yttrium iron garnet onto nongarnet substrates with faster deposition rates and high reliability," Appl. Phys. Lett. **87**(12), 121111 (2005).
10. Y.-Q. Li, M. Cherif, J. Huang, W. Liu, and Q. Chen, "Metalorganic chemical vapor deposition of magneto-optical Ce:YIG thin films," MRS Proceedings **517**, 449 (1998).
11. M. C. Sekhar, J.-Y. Hwang, M. Ferrera, Y. Linzon, L. Razzari, C. Harnagea, M. Zaezjev, A. Pignolet, and R. Morandotti, "Strong enhancement of the Faraday rotation in Ce and Bi comodified epitaxial iron garnet thin films," Appl. Phys. Lett. **94**(18), 181916 (2009).
12. M. Sekhar, M. R. Singh, S. Basu, and S. Pinnepalli, "Giant Faraday rotation in $Bi_xCe_{3-x}Fe_5O_{12}$ epitaxial garnet films," Opt. Express **20**(9), 9624–9639 (2012).
13. M.-C. Tien, T. Mizumoto, P. Pintus, H. Kromer, and J. E. Bowers, "Silicon ring isolators with bonded nonreciprocal magneto-optic garnets," Opt. Express **19**(12), 11740–11745 (2011).
14. P. Pintus, F. Di Pasquale, and J. E. Bowers, "Design of TE ring isolators for ultra low loss Si3N4 waveguides based on the finite element method," Opt. Lett. **36**, 4599–4601 (2011).

15. J. F. Bauters, M. J. R. Heck, D. John, D. Dai, M.-C. Tien, J. S. Barton, A. Leinse, R.-G. Heideman, D. J. Blumenthal, and J. E. Bowers, "Ultra-low-loss high-aspect-ratio Si3N4 waveguides," Opt. Express **19**(4), 3163–3174 (2011).
16. L. D. Landau and E. M. Lifshits, *Electrodynamics of Continuous Media*. (Pergamon, 1960).
17. H. Dötsch, N. Bahlmann, O. Zhuromskyy, M. Hammer, L. Wilkens, R. Gerhardt, P. Hertel, and A. F. Popkov, "Applications of magneto-optical waveguides in integrated optics: review," J. Opt. Soc. Am. B **22**, 240–253 (2005).
18. O. Zhuromskyy, H. Dötsch, M. Lohmeyer, L. Wilkens, and P. Hertel, "Magnetooptical waveguides with polarization-independent nonreciprocal phaseshift," J. Lightwave Technol. **19**(2), 214–221 (2001).
19. M. Gomi, H. Furuyama, and M. Abe, "Strong magneto-optical enhancement in highly Ce-substituted iron garnet films prepared by sputtering," J. Appl. Phys. **70**(11), 7065 (1991).
20. G. J. Gabriel and M. E. Brodwin, "The solution of guided waves in inhomogeneous anisotropic media by perturbation and variational method," IEEE Trans. Microw. Theory Tech. **13**(3), 364–370 (1965).
21. O. Zhuromskyy, M. Lohmeyer, N. Bahlmann, H. Dötsch, P. Hertel, and A. F. Popkov, "Analysis of polarization-independent Mach-Zehnder-type integrated optical isolator," J. Lightwave Technol. **17**(7), 1200–1205 (1999).
22. A. Konrad, "High-order triangular finite elements for electromagnetic waves in anisotropic media," IEEE Trans. Microw. Theory Tech. **25**(5), 353–360 (1977).
23. J. Jin, *The Finite Element Method in Electromagnetics*, second edition. (Wiley, 2002).
24. F. Morichetti, A. Canciamilla, C. Ferrari, M. Torregiani, A. Melloni, and M. Martinelli, "Roughness induced backscattering in optical silicon waveguides," Phys. Rev. Lett. **104**(3), 033902 (2010).
25. B. E. Little, J.-P. Laine, and S. T. Chu, "Surface-roughness-induced contradirectional coupling in ring and disk resonators," Opt. Lett. **22**(1), 4–6 (1997).
26. F. Morichetti, A. Canciamilla, M. Martinelli, A. Samarelli, R. M. De La Rue, M. Sorel, and A. Melloni, "Coherent backscattering in optical microring resonators," Appl. Phys. Lett. **96**(8), 081112 (2010).
27. J. Capmany, P. Muñoz, J. D. Domenech, and M. A. Muriel, "Apodized coupled resonator waveguides," Opt. Express **15**(16), 10196–10206 (2007).
28. D.-X. Xu, A. Densmore, P. Waldron, J. Lapointe, E. Post, A. Delâge, S. Janz, P. Cheben, J. H. Schmid, and B. Lamontagne, "High bandwidth SOI photonic wire ring resonators using MMI couplers," Opt. Express **15**(6), 3149–3155 (2007).
29. US Patent Application US 2012/0002914 A1, Inventors: H. Kroemer, J. E. Bowers, and M.-C. Tien, Pub. Date: 5th January 2012.
30. T. Sekijima, H. Itoh, T. Fujii, K. Wakino, and M. Okada, "Influence of growth atmosphere on solubility limit of Ce^{3+} ions in Ce-substituted fibrous yttrium iron garnet single crystals," J. Cryst. Growth **229**(1-4), 409–414 (2001).

1. Introduction

In the last decades, a great effort has been devoted to the integration of optical components on a single chip. The miniaturization of non-reciprocal devices, key elements to reduce the feedback noise and allow serial integration of active and passive photonic components, is very challenging and has attracted a great deal of attention [1,2].

Recently, magneto-optical resonators in 2D photonic crystals have been proposed to realize planar and compact optical circulators [3,4]; however, photonic crystals require a complex design with precise magnetization domain control over micron scale, making such components rather difficult to be manufactured. Alternatively, non-reciprocal phase shift effect (NRPS) can be effectively employed to devise optical circulators based on Mach-Zehnder interferometers, where proper phase shifter generates constructive interference for forward light and destructive interference for backward light. Exploiting this solution, Takei and Mizumoto have lately designed and simulated a four-port and a three-port optical circulators, where a non-reciprocal phase shifter can be obtained directly bonding cerium-substituted yttrium iron garnet (Ce:YIG) on standard silicon waveguide [5]. Although those devices exhibit a low crosstalk (below −20dB), they are however relatively long (about 420μm) and work only for the TM polarized mode.

In this work, we present two four-port integrated optical circulators based on compact and wavelength selective microring resonators for TE and TM modes, respectively. Considering the recent fabrication developments for efficiently integrating Ce:YIG on silicon nitride film [6,7], we have designed and optimized the ring cross-section to maximize the magneto-optic effect for both polarizations.

The TE-mode circulator, which is schematically shown in Fig. 1, consists of two straight waveguides laterally (or vertically [8]) coupled to a ring resonator that can be manufactured using silicon nitride (Si_3N_4) on a silicon oxide substrate. After etching of the internal side of

the ring, a thin (25nm) yttrium iron garnet (YIG) layer can be either deposited on silicon nitride or directly on silica layer, using the pulse laser deposition (PLD) technique followed by a rapid thermal annealing at high temperatures to crystallize it. Note that a Ce:YIG layer can be grown with the same deposition technique on the YIG seed layer. Such a process, which is described in [7], can preserve the target stoichiometry and enable good quality Ce:YIG. Indeed, the Faraday rotation of such a magneto-optic film is over 4000deg/cm, which is higher than the one of polycrystalline garnet films grown by sputtering [9] and similar to metal organic chemical vapor deposition (MOCVD) on gadolinium gallium garnet substrates [10]. Moreover, the same deposition technique can be used for similar magneto-optic material, like cerium and bismuth substituted iron garnet materials, which are characterized by a higher Faraday rotation constant (e.g., θ_F between 9100deg/cm [11] and 11000deg/cm [12]).
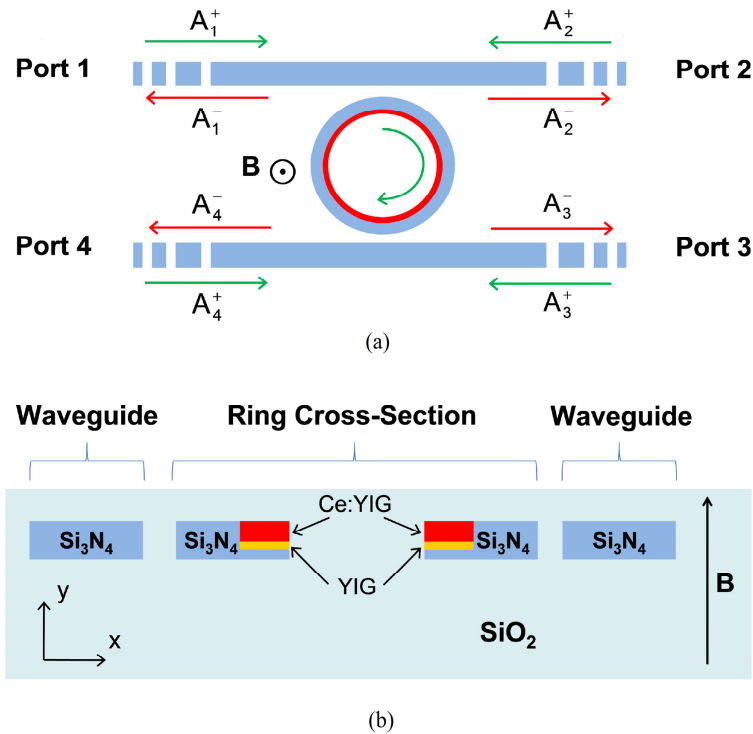

(a)

(b)

Fig. 1. Schematic structure of the TE-mode four-port optical circulator, Top view (a) and cross-section (b).

For the TM circulator, the ring cross-section is fully planar, and a YIG and Ce:YIG layers can be deposited on the silicon nitride waveguide without any etching.

The schematic views of the ring cross sections for the TE and TM circulators are shown in Figs. 2(a) and 2(b), respectively. In the same Figs., we have also drawn the external magnetic field directions, which induce the non-reciprocal phase shift for the two polarizations.
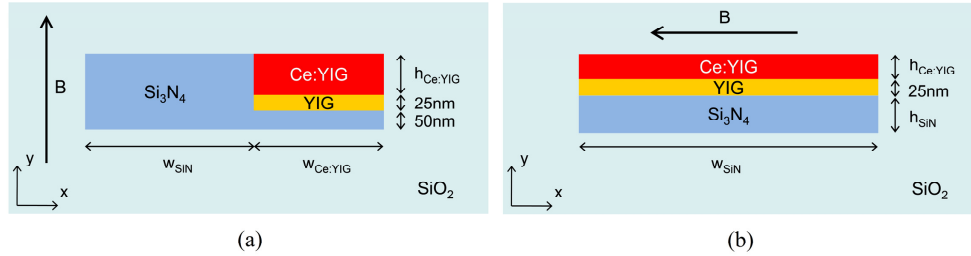
Fig. 2. Ring-cross section and external magnetic field direction for the TE-mode circulator (a) and TM-mode circulator (b).

By applying a transverse magneto-static field with respect to the direction of propagation (radial for the TM-circulator and vertical for the TE case), the symmetry of the ring is broken by the NRPS effect. The clock-wise (CW) and the counter-clock-wise (CCW) propagation constants for the TE (TM) mode will be significantly differentiated, resulting in a different resonant wavelength for the two directions [13,14]. The different frequency response of the ring is used to filter out the backward light providing the required circulating functions.

The closed four-port characteristics of the two devices can be easily verified. Indeed, the input-output circulator relations are Port 1→Port 2→Port 3→Port 4→Port 1, when the ring is resonating at the CCW resonance wavelength. Vice versa, at the CW resonance wavelength, input-output ports are connected as Port 1→Port 4→Port 3→Port 2→Port 1.

Note that the proposed devices combine the benefit of low loss silicon nitride waveguides [15] with the non-reciprocal properties of the Ce:YIG material. Moreover, high aspect ratio Si_3N_4 waveguides are characterized by material stability, high refractive index regularity and low cross-polarization [15], making these devices particularly attractive.

Several different applications of such integrated devices can be envisaged for communication and for sensing as well. The devices can be successfully used as input/output isolators for integrated optical amplifiers as well as a compact de-interleaver for wavelength division multiplexing (WDM) applications. For example, a WDM signal injected from Port 1, can be effectively separated into two interleaved grids at Port 2 and Port 4 respectively, providing simultaneously high input-output isolation. By designing the microring structure such that the resonance wavelength split induced by the non-reciprocal effect $\Delta\lambda$ corresponds to the WDM channel spacing (e.g., 50 GHz), and with a ring resonator free spectral range (FSR) which is twice $\Delta\lambda$, the WDM input channels from Port 1 can be separated into Port 2 (even channels) and Port 4 (odd channels), with high isolation between input and output ports. Note that while $\Delta\lambda$ is related to the Faraday constant, the FSR depends on the ring radius, so the two parameters can be optimized separately.

Such microring based devices can be also successfully employed to isolate integrated optical amplifiers and lasers from the detrimental back reflected light; in these applications the resonance wavelength split induced by the non-reciprocal effect should be much larger than the signal bandwidth to separate the waves in the propagating and counter-propagating directions. For example, considering a signal bandwidth of 10GHz, $\Delta\lambda$ should be larger than 0.2nm (~25GHz). For these applications, the ring radius can be further reduced in order to decrease the circulator footprint. Moreover, a cascaded of non-reciprocal rings can be effectively used to increase the isolation, and enlarge the bandwidth, improving the device performance.

2. Theoretical model

2.1 Modal analysis

The devices we propose can be manufactured exploiting a silicon nitride platform ($n_{Si3N4} = 1.99$). Thanks to the recent technological improvements [7], it is possible to deposit a thin YIG layer ($n_{YIG} = 2.19$) on a Si_3N_4 substrate and a Ce:YIG layer can then be grown ($n_{Ce:YIG} = 2.22$). The whole structure is buried in a silica coating ($n_{SiO2} = 1.46$). The mode profile and

the resonance wavelength shift have been estimated employing an *equivalent straight waveguide* with the same ring cross-section. Such approximation provides small errors thanks to the high SOI index contrast and consequently the high field confinement factor even in small radius rings [14]. The electromagnetic fields of the guided modes can be written in the form $\underline{E}(x,y)e^{i(\omega t-\beta z)}$, $\underline{H}(x,y)e^{i(\omega t-\beta z)}$, where ω denotes the angular frequency and β is the mode propagation constant.

By applying an external magnetic field, the magneto-optical garnet (Ce:YIG) results polarized and its relative permittivity tensor assume the following form

$$\underline{\underline{\varepsilon}}_r = n^2_{Ce:YIG}\begin{pmatrix} 1 & 0 & 0 \\ 0 & 1 & 0 \\ 0 & 0 & 1 \end{pmatrix} + K\begin{pmatrix} 0 & M_z & -M_y \\ -M_z & 0 & M_x \\ M_y & -M_x & 0 \end{pmatrix}, \qquad (1)$$

where M_x, M_y and M_z denote the components of the magnetization and $K = K' + jK''$ is a complex material parameter. The real part of K is related to the Faraday ellipticity and it is negligible in Ce:YIG, while K'' is linked to the NRPS effect [16,17]. If the magnetization is saturated, the off-diagonal elements of the permittivity tensor are related to the specific Faraday rotation θ_F^j, j = x,y,z by the following relation

$$K''M_j = \frac{2\,\theta_F^j\,n_{Ce:YIG}}{k_0}, \qquad (2)$$

where k_0 is the vacuum wave number [17,18]. In our case, an external magnetic flux density of~50 Gauss is needed to saturate the Ce:YIG [13]. Moreover, as the Faraday rotation is proportional to the substitution level of Cerium in the crystal [19], the non-reciprocal effect can be enhanced by increasing the doping level.

The off-diagonal entries of the permittivity matrix are responsible of the non-reciprocal phase shift effect. When $K''M_j$ are much smaller than the diagonal entries (i.e., $(n_{Ce:YIG})^2$), the shift between forward and backward propagation constants can be estimated by applying the Schrödinger perturbation theory [20]. Using this approach, the electromagnetic fields are computed neglecting the Ce:YIG anisotropy, and the phase shift for the two modes are computed using the following formulas [21]

$$\Delta\beta_{TE} \cong -\frac{2\omega\varepsilon_0}{\beta_{TE}N}\iint K''M_y E_x^* \partial_x E_x dxdy \quad \text{and} \quad \Delta\beta_{TM} \cong \frac{2\omega\varepsilon_0}{\beta_{TM}N}\iint K''M_x E_y^* \partial_y E_y dxdy, (3)$$

where ε_0 is the vacuum permittivity and

$$N = \frac{1}{2}\iint \left[\underline{E}\times\underline{H}^* + \underline{E}^*\times\underline{H}\right]_z dxdy. \qquad (4)$$

Note that the Cartesian axes (x,y) in our coordinate system are swapped with respect to the ones in Zhuromskyy *et al.* [21], so the formula for TE and TM NRPS are switched.

As shown in Eqs (3), the TE-mode phase shift depends on M_y (i.e., external magnetic field along vertical direction), while the TM-mode phase shift is related to M_x (i.e., external magnetic field along horizontal direction). Let us focus our attention on the TE-case: $\Delta\beta_{TE}$ depends on the integral of $E_x^*\partial_x E_x$. If the core of the waveguide is not homogeneous along the horizontal axis (see Fig. 2(a)), E_x is discontinuous and its derivarive along x, $\partial_x E_x$, becomes very large. Vice versa, $\Delta\beta_{TM}$ is proportional to the integral of $E_y^*\partial_y E_y$, which becomes very large when the waveguide core is discontinuous along the vertical direction (see Fig. 2(b)). These physical considerations well explain the geometries of the two non-reciprocal waveguide structures proposed for TE and TM modes. Also note that the largest phase shift will occur in structures where the boundary separating the regions with different Faraday rotation is placed at the mode field maximum [21].

In this work, we directly solve the Maxwell's equations to compute the non reciprocal phase shift without introducing any approximation. All the material involved are isotropic with the only exception of the Ce:YIG, which has a Hermitian permittivity tensor. It can be easily proved that the electric and magnetic field of the travelling waves can be written as [22,23]:

$$\underline{E} = \left[E_x(x,y)\underline{i}_x + E_y(x,y)\underline{i}_y + jE_z(x,y)\underline{i}_z \right]e^{j\omega t - j\beta z}, \tag{5.a}$$

$$\underline{H} = \left[H_x(x,y)\underline{i}_x + H_y(x,y)\underline{i}_y + jH_z(x,y)\underline{i}_z \right]e^{j\omega t - j\beta z}, \tag{5.b}$$

where all the field components (E_x, E_y, E_z) and (H_x, H_y, H_z) are real. To compute the modes of the equivalent straight waveguide, we have numerically solved the curl-curl equation for the magnetic field $\underline{H}$ using a node-based full vectorial finite element method (FEM) [22,23]:

$$\nabla \times \left(\underline{\underline{\varepsilon}}_r^{-1} \nabla \times \underline{H} \right) - k_0^2 \underline{H} = 0. \tag{6}$$

From Eq. (6), we have calculated the field $\underline{H}^{\pm}$, the propagation constants $\beta^{\pm}(\lambda)$ and the effective index $n^{\pm}_{eff} = \beta^{\pm}(\lambda)/k_0$ as a function of the wavelength, where the superscript $\pm$ indicates the CW and CCW modes. Note that the different phase velocities in the two directions result into different resonant wavelengths. Labeling with λ^+ and λ^- the CW and the CCW resonance wavelengths, the split is $\Delta\lambda = |\lambda^+ - \lambda^-| = \lambda\Delta n_{eff}/n_g$ where n_g is the average group index with respect to the two directions: $n_g = (n^+_g + n^-_g)/2$, where $n^{\pm}_g = n^{\pm}_{eff} - \lambda \cdot \partial n^{\pm}_{eff}/\partial\lambda$, for the two directions. The propagation constant $\beta^{\pm}(\lambda)$ are then used to compute the scattering matrix of the two devices, as it will be described in the next subsection.

Solving directly Eq. (6) including the magneto-optic effect provides more accurate results than the perturbation theory, in which the fields are computed assuming all material isotropic and then using Eq. (3). Indeed, while the former method introduces only numerical error, the latter is based on an approximated solution. The two approaches have been compared in [13].

2.2 Scattering matrix

Labeling with A^+_i the incident wave from Port i and with A^-_k the scattered wave from Port k, with i,k = 1,2,3,4, we can relate them using the scattering matrix formalism:

$$\begin{pmatrix} A^-_1 \\ A^-_2 \\ A^-_3 \\ A^-_4 \end{pmatrix} = \begin{pmatrix} S_{11} & S_{12} & S_{13} & S_{14} \\ S_{21} & S_{22} & S_{23} & S_{24} \\ S_{31} & S_{32} & S_{33} & S_{34} \\ S_{41} & S_{42} & S_{43} & S_{44} \end{pmatrix} \begin{pmatrix} A^+_1 \\ A^+_2 \\ A^+_3 \\ A^+_4 \end{pmatrix}. \tag{7}$$

Those coefficients depend on the attenuation (α), the propagation constant (β), the ring radius (R), and the ring-waveguide power coupling ratio (κ), defined as the fraction of power coupled to the ring per round trip. When no power is coupled between ring and waveguide (e.g., large distance) $\kappa = 0$, vice versa when all the power is transferred from the waveguide to the ring, $\kappa = 1$.

Note that the waveguide back-scattering is related to the waveguide width, to the group index and to the waveguide propagation loss [24]. In ring-resonators, back-reflection might be significantly enhanced by the ring surface roughness, when the ring-waveguide power coupling ratio κ is smaller than the surface-roughness-induced reflectivity [25,26]. The use of Si_3N_4 waveguides, characterized by high aspect ratio, lower index-contrast than silicon waveguide, and low-loss, allow us to consider negligible the back-scattering coefficients along the diagonal (i.e., $S_{11} = S_{22} = S_{33} = S_{44} = 0$) [15]. Moreover, as explained in the introduction, the light injected from Port 1 can propagate only through Port 2 and Port 4,

which implies $S_{13} = 0$. For the same reason $S_{24} = S_{31} = S_{42} = 0$. Those coefficients can be computed using the transfer matrix method [27].

If the coupling coefficients between the ring and the two longitudinal waveguides are the same ($\kappa_1 = \kappa_2 = \kappa$), we have that $S_{32} = S_{14}$, $S_{34} = S_{12}$, $S_{43} = S_{21}$, $S_{41} = S_{23}$ due to the symmetry. Thanks to the previous simplifications, the scattering matrix can be re-written as:

$$
\begin{pmatrix} A_1^- \\ A_2^- \\ A_3^- \\ A_4^- \end{pmatrix} = \begin{pmatrix} 0 & S_{12} & 0 & S_{14} \\ S_{43} & 0 & S_{41} & 0 \\ 0 & S_{14} & 0 & S_{12} \\ S_{41} & 0 & S_{43} & 0 \end{pmatrix} \begin{pmatrix} A_1^+ \\ A_2^+ \\ A_3^+ \\ A_4^+ \end{pmatrix}
\tag{8}
$$

where only four coefficients are independent. Note that an ideal circulator would have S_{12} and S_{41} equal to zero, while S_{14} and S_{43} would be equal to one. Changing the ring-waveguide distance, we can vary the ring-waveguide power coupling ratio κ to optimize the scattering coefficients. Because κ is a very sensitive parameter, the ring-waveguide coupling can be made more robust using a multi-mode-interference (MMI) coupler [28].

3. Numerical results

3.1 Modal analysis and cross-section optimization

To maximize the resonance wavelength split between the CW and the CCW modes and guarantee the single mode regime, we have optimized the geometrical parameter of the ring. For the TE-circulator, we have considered two different rings, which are 300nm and 400nm thick, and we have varied the silicon nitride (w_{SiN}) and magneto-optical material ($w_{Ce:YIG}$) widths, as defined in Fig. 2(a). The results of the analysis are shown in Figs. 3(a) and 3(b), which refer to a 300nm and 400nm thick equivalent waveguide, respectively. In the two Figs. a dashed line is used to separate two different operating regions: while the upper region above the dashed line represents single mode waveguide regime, the lower region refers to multi-modes rings.

From the FEM computation, the maximum of the nonreciprocal phase shift effect in a 400nm thick ring can be reached with a 440nm-wide Si_3N_4 and a 350nm-wide Ce:YIG layers. Note that a small aspect ratio waveguide results in higher waveguide loss due to the side-wall roughness. For this reason, in our analysis, we have consider a larger cross-section (w_{SiN} = 550nm, $w_{Ce:YIG}$ = 350nm) which is not the optimum one, but can still guarantee a high value for the resonance wavelength split ($\Delta\lambda$ ~0.29nm, corresponding to ~36GHz).

Moreover, a higher resonance split can be reached co-doping the garnet with bismuth [11]. Enhanced Faraday rotation values within the range 10000-11000 degree/cm have been measured in thin films of $Bi_xCe_{3-x}Fe_5O_{12}$ prepared by using PLD [12]. With the same cross-section, such material would allow $\Delta\lambda$ higher than 0.8nm, which means a resonance split larger than 100GHz. In addition, a larger resonance wavelength split would imply higher isolation, as it will be shown in the following section.
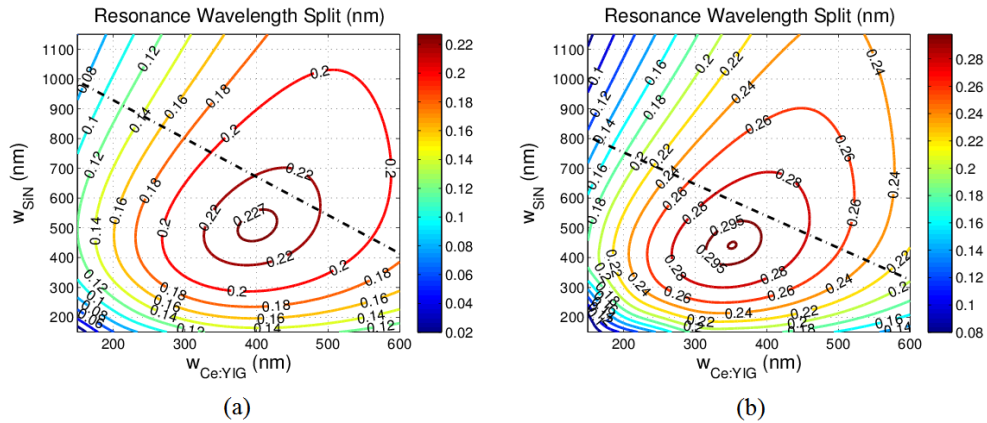
Fig. 3. Resonance wavelength split for the TE-circulator as a function of the silicon nitride (w_{SiN}) and the magneto-optical material width ($w_{Ce:YIG}$). Figures 3(a) and 3(b) refer to a 300nm and 400nm thick waveguide, respectively.

A similar analysis has been carried for the TM mode device. In this case, we have analyzed a 1.15μm and a 850nm wide cross-sections. For both cases, we have computed the resonance wavelength split for different silicon nitride (h_{SiN}) and magneto-optical material ($h_{Ce:YIG}$) layer thickness, as reported in Fig. 2(b). The results in Fig. 4(a) show that the 850nm-wide ring is single mode even for thick Si_3N_4 and Ce:YIG layers. Assuming $h_{SiN} = 200$nm and $h_{Ce:YIG} = 175$nm, a resonance wavelength split $\Delta\lambda \sim 0.325$nm can be reached. Note that the main issue of this device is related to the radial magnetostatic field application, which can be done using a cylindrical magnet [13] or multi-turn coils above the ring [29].
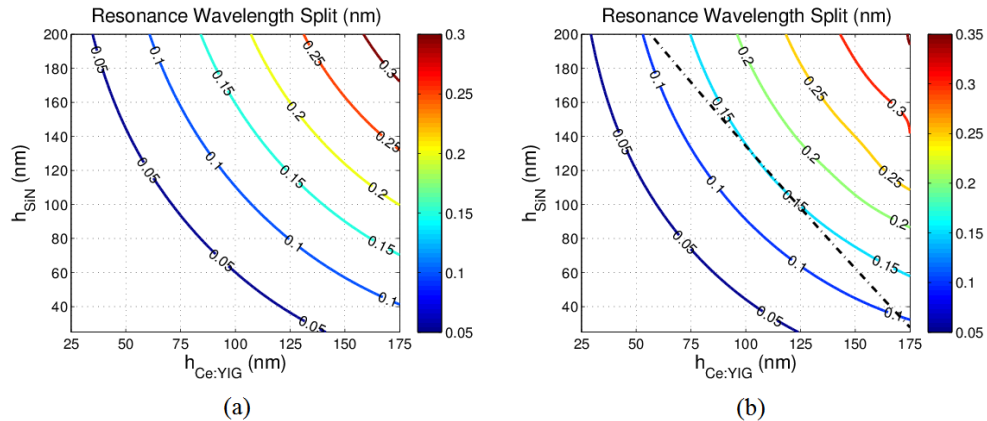

Fig. 4. Resonance wavelength split for the TM-circulator as a function of the silicon nitride (h_{SiN}) and the magneto-optical material thickness ($h_{Ce:YIG}$). Figure 4(a) and 4(b) refer to a 850nm and 1.15μm large waveguide, respectively.

For the optimized ring cross sections previously identified, the field confinement in the MO material is less than 24% for the TE-circulator and less than 22% for the TM-circulator. Figures 5(a) and 5(b) show the spatial distributions of the principal TE and TM mode components on the two waveguide cross-sections, which have been computed solving Eq. (4).
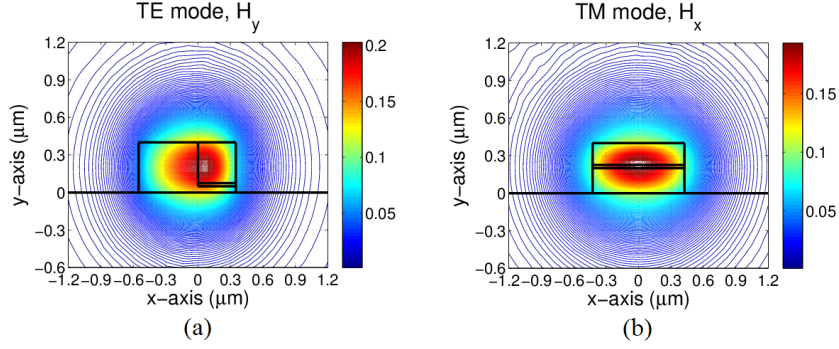
Fig. 5. Magnetic field profile of the principal component for TE-mode (a) and TM-mode (b) in the two circulators, respectively.

Being the optical absorption in the crystal as low as 4dB/cm [30], we have considered two possible values of ring-loss: $\alpha_{rr} = 1$dB/cm and $\alpha_{rr} = 3$dB/cm, while a loss of 0.1dB/cm has been assumed for the Si_3N_4-waveguides which are coupled to the ring.

Concerning the ring footprint, its radius should be chosen such that the spectra for the forward and backward resonances are offset by more than half of FSR, which means:

$$FSR = \frac{\lambda^2}{2\pi R n_g} \geq 2\,\varDelta\lambda \quad \Rightarrow \quad R \leq \frac{\lambda^2}{4\pi\,\varDelta\lambda\,n_g}. \tag{9}$$

For the TE and TM ring cross-sections previously considered, the maximal ring radius R_M is equal to 306.5μm for the TE-circulator and equals 284.5μm for the TM-circulator. When $R = R_M$, the forward and backward spectra are interleaved and shifted by $\varDelta\lambda$. As we have mentioned in the introduction, by engineering the resonance wavelength split we can design an integrated de-interleaver which can provide high isolation between its input and output ports. For general circulator applications, we can also consider smaller ring radius in order to reduce the footprint. In the following section, we will consider $R = 25$μm.

3.2 Scattering matrix analysis

Let us first focus on the TE circulator; Figs. 6(a)-6(d) show the four independent coefficients S_{12}, S_{14}, S_{41}, and S_{43} computed for $\alpha_{rr} = 1$dB/cm and different κ as a function of the wavelength. As we can see, the bigger is κ, the larger is the bandwidth. Indeed, if the values of κ are greater than the intrinsic cavity loss per round trip time $\gamma_0 = 2\pi R\alpha_{rr}$, the ring is over-coupled.

For λ equal to the CW resonant wavelength, we have computed the four independent scattering coefficients as a function of the power coupling ratio κ, as shown in Figs. 7(a) and 7(b). The coefficients S_{43} and S_{14} become close to 0dB as the value of κ increases. Vice versa, S_{12} and S_{41} are pretty small in amplitude. By increasing κ, we increase the power exchanged from Port 1 to Port 4, while S_{12} decreases and S_{41} becomes larger. As ideal circulators are characterized by $S_{12} = S_{41} = 0$, we have chosen κ in such a way to keep both of them as small as possible at the same time. From Fig. 7(a), the optimum value of κ is ~2.0%, leading to $|S_{14}| = -0.74$dB, $|S_{43}| = -0.03$dB and $|S_{12}| = |S_{41}| = -21.9$dB. For that value of κ, the 3dB bandwidth is as large as 6.3GHz as it can be clearly seen in Fig. 7(c).
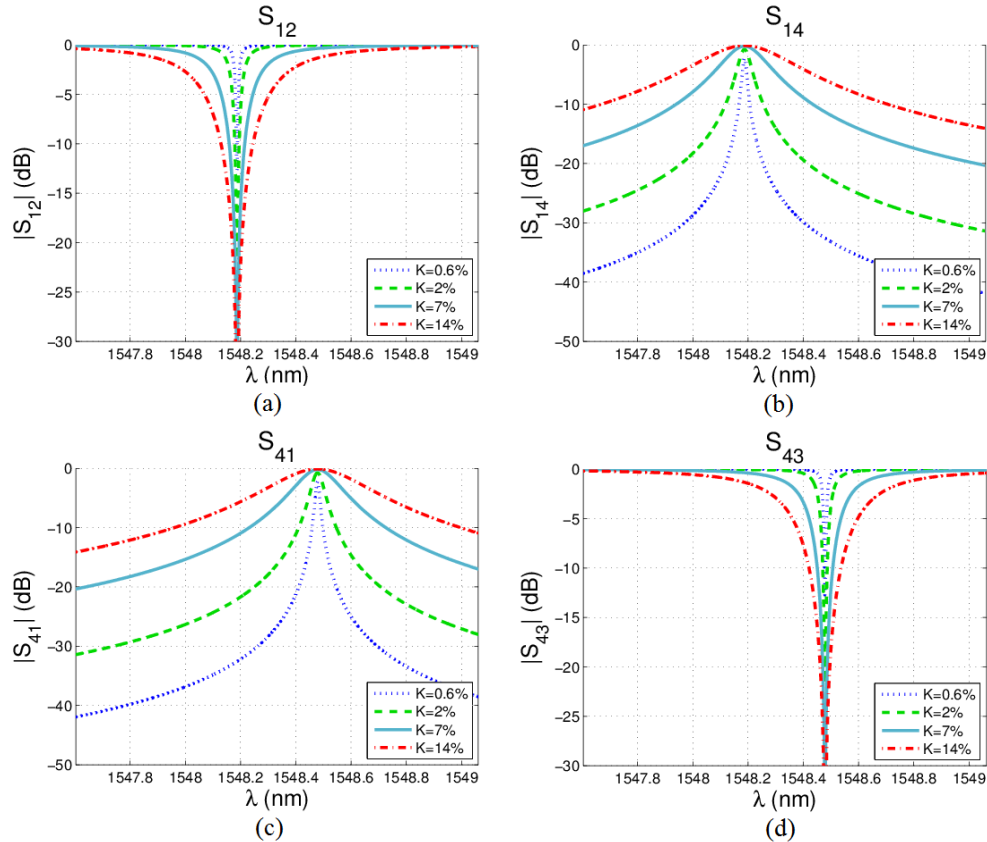
Fig. 6. Scattering coefficients as a function of wavelength λ and power coupling coefficients κ.

In order to improve the circulator performance, we can alternatively increase the power exchanged between the two waveguides by coupling the two buses through an array of ring resonators. We can clearly see that $|S_{12}|$ and $|S_{41}|$ decrease with the number of rings while $|S_{14}|$ and $|S_{43}|$ have opposite behavior. The last two parameters (S_{14} and S_{43}) are the insertion losses of the device between two connected ports, which are quite small in all cases.
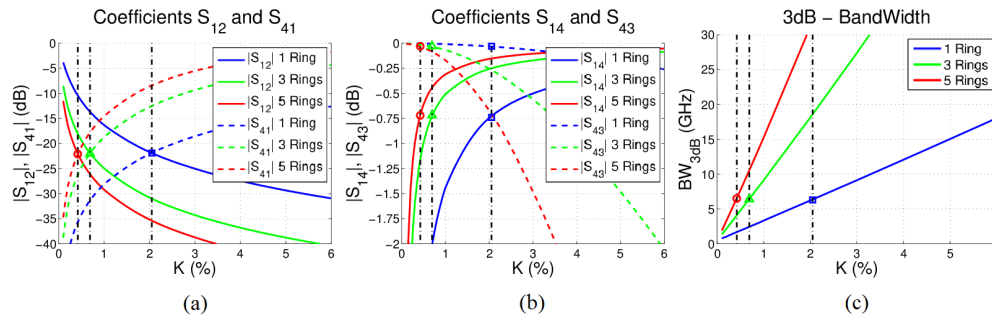

Fig. 7. Scattering coefficients at CW resonant frequency as a function of κ ($\alpha_{rr} = 1$dB/cm) for $R = 25\mu$m.

For comparison, we have also simulated the TE-circulator behavior for a larger ring radius ($R = 300\mu$m). In this case, the optimum value of κ is larger in order to compensate for the bigger cavity loss. The results are shown in Figs. 8(a), 8(b), and 8(c).
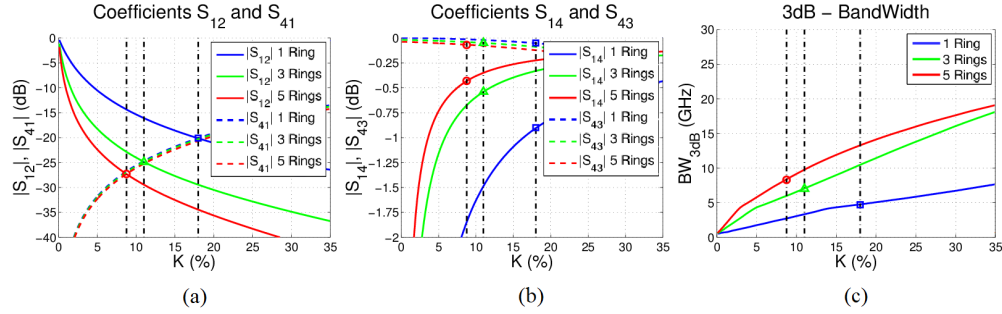
Fig. 8. Scattering coefficients at CW resonant frequency as a function of κ (α_{rr} = 1dB/cm)) for $R = 300\mu$m.

Table 1 reports the circulator scattering coefficients at the CW ring resonance for two different ring losses, with one, three and five rings, respectively. Note that we have fixed the optical path distance between the rings equal to πR so that the fields interfere constructively at the resonance wavelength. In the same table we have also reported the 3dB bandwidth, which is comparable with the values reported in [3].

It is useful to point out that the full width at half maximum bandwidth is proportional to the sum of κ and γ_0; as γ_0 is very small compared to the power coupling ratio for the ring radius we are considering, the 3dB bandwidth is then almost proportional to κ. Note that we can broaden the circulator bandwidth by increasing the value of κ, bigger value of which can still guarantee small values for S_{14} and S_{43}.

Table 1. TE-circulator scattering coefficients at CW ring resonance

	Loss	#Rings	κ	$|S_{12}|$	$|S_{14}|$	$|S_{43}|$	$|S_{41}|$	BW$_{3dB}$
Ideal Circulator	-	-	-	-Inf	0	0	-Inf	-
$R = 25\mu$m	α_{rr} = 1dB/cm	1	2.05%	−21.9dB	−0.74dB	−0.03dB	−21.9dB	6.3GHz
		3	0.69%	−22.0dB	−0.72dB	−0.03dB	−22.0dB	6.4GHz
		5	0.42%	−22.1dB	−0.72dB	−0.03dB	−22.1dB	6.5GHz
	α_{rr} = 3dB/cm	1	3.46%	−17.4dB	−1.27dB	−0.11dB	−17.4dB	11.5GHz
		3	1.21%	−17.5dB	−1.25dB	−0.12dB	−17.5dB	12.1GHz
		5	0.71%	−17.6dB	−1.23dB	−0.13dB	−17.6dB	11.9GHz
$R = 300\mu$m	α_{rr} = 1dB/cm	1	18.0%	−20.1dB	−0.9dB	−0.05dB	−20.1dB	4.7GHz
		3	11.0%	−24.9dB	−0.54B	−0.05dB	−24.9dB	7.0GHz
		5	8.75%	−27.3dB	−0.43dB	−0.07dB	−27.3dB	8.3GHz
	α_{rr} = 3dB/cm	1	28.2%	−15.7dB	−1.58dB	−0.17dB	−15.7dB	6.9GHz
		3	18.0%	−20.3dB	−0.94dB	−0.14dB	−20.3dB	10.8GHz
		5	14.5%	−22.7dB	−0.76dB	−0.17dB	−22.7dB	11.5GHz

Similar results have been achieved for the TM-circulator structure and they are reported in Table 2. Note that the cross section we have considered for the TM case allows a resonance wavelength split slightly larger than the one for the TE case ($\Delta\lambda_{TM}$ = 0.325nm and $\Delta\lambda_{TE}$ = 0.292nm). For this reason the circulator performance is slightly improved. It is interesting to see how the scattering coefficients and the bandwidth can be enhanced by using a magneto-optical material characterized by a higher Faraday rotation constant as it is for the $Bi_xCe_{3-x}Fe_5O_{12}$ (θ_F = 11000deg/cm [12]). This material has almost the same refractive index and will allow a resonance wavelength split as large as 0.8nm. The results of this analysis are shown in Table 3. Comparing those results with the one in Table 1, we can clearly see lower

values for $|S_{12}|$ and $|S_{41}|$, which have been decreased by more than 4dB. Moreover, because the ideal power coupling coefficients are bigger, we also achieve a larger 3dB bandwidth. Also in this case, relaxing the constraint on S_{12} and S_{41}, it is possible to further broaden the device bandwidth.

Table 2. TM-circulator scattering coefficients at CW ring resonance

	Loss	#Rings	κ	$|S_{12}|$	$|S_{14}|$	$|S_{43}|$	$|S_{41}|$	BW$_{3dB}$
Ideal Circulator	-	-	-	-Inf	0	0	-Inf	-
$R = 25\mu m$	$\alpha_{rr} =$ 1dB/cm	1	2.12%	−22.1dB	−0.72dB	−0.03dB	−22.1dB	6.9GHz
		3	0.71%	−22.1dB	−0.71dB	−0.03dB	−22.1dB	7.0GHz
		5	0.44%	−22.3dB	−0.70dB	−0.03dB	−22.3dB	7.2GHz
	$\alpha_{rr} =$ 3dB/cm	1	3.55%	−17.6dB	−1.24dB	−0.10dB	−17.6dB	12.4GHz
		3	1.25%	−17.7dB	−1.24dB	−0.12dB	−17.7dB	13.1GHz
		5	0.73%	−17.8dB	−1.22dB	−0.10dB	−17.8dB	12.9GHz

Table 3. TE-circulator fabricated with Bi$_x$Ce$_{3-x}$Fe$_5$O$_{12}$ instead of Ce:YIG ($\theta_F =$ 11000deg/cm [12])

	Loss	#Rings	κ	$|S_{12}|$	$|S_{14}|$	$|S_{43}|$	$|S_{41}|$	BW$_{3dB}$
Ideal Circulator	-	-	-	-Inf	0	0	-Inf	-
$R = 25\mu m$	$\alpha_{rr} =$ 1dB/cm	1	3.40%	−26.0dB	−0.45dB	−0.01dB	−26.0dB	10.5GHz
		3	1.29%	−26.6dB	−0.43dB	−0.01dB	−26.6dB	11.9GHz
		5	0.88%	−28.1dB	−0.35dB	−0.01dB	−28.1dB	13.7GHz
	$\alpha_{rr} =$ 3dB/cm	1	5.68%	−21.4dB	−0.78dB	−0.04dB	−21.4dB	18.5GHz
		3	2.08%	−22.0dB	−0.72dB	−0.04dB	−22.0dB	20.3GHz
		5	1.56%	−23.4dB	−0.67dB	−0.04dB	−23.4dB	25.7GHz

4. Conclusion

In this work, we have presented the design of two four-port integrated optical circulators for TE and TM modes, which combine the advantages of new low-loss silicon nitride waveguides with the non-reciprocal properties of magneto-optical materials growth by pulse laser deposition. Based on the recent technological improvement in the monolithic integration of Ce:YIG on SOI [7], we have designed new integrated circulators which can be effectively used in integrated optics. The resonance wavelength split has been maximized with respect to the ring cross-section and the scattering coefficients have been optimized with respect to the ring-waveguide power coupling ratio κ. Finally, we have investigated the performance of magneto-optical material which exhibits a giant Faraday rotation, like Bi$_x$Ce$_{3-x}$Fe$_5$O$_{12}$ [12]. The results show that such a material can be exploited to further improve the performance of the integrated devices.